

Faraday waves in a Hele-Shaw cell

Jing Li, Xiaochen Li, Kaijie Chen, Bin Xie, and Shijun Liao

Citation: *Physics of Fluids* **30**, 042106 (2018); doi: 10.1063/1.5022424

View online: <https://doi.org/10.1063/1.5022424>

View Table of Contents: <http://aip.scitation.org/toc/phf/30/4>

Published by the *American Institute of Physics*



**COMPLETELY
REDESIGNED!**

**PHYSICS
TODAY**

Physics Today Buyer's Guide
Search with a purpose.

Faraday waves in a Hele-Shaw cell

Jing Li,¹ Xiaochen Li,² Kaijie Chen,¹ Bin Xie,¹ and Shijun Liao^{1,a)}

¹State Key Laboratory of Ocean Engineering, School of Naval Architecture, Ocean and Civil Engineering, Shanghai Jiao Tong University, Shanghai 200240, China

²School of Civil Engineering and Transportation, South China University of Technology, Guangzhou 510641, China

(Received 15 January 2018; accepted 10 April 2018; published online 24 April 2018)

We investigate Faraday waves in a Hele-Shaw cell via experimental, numerical, and theoretical studies. Inspired by the Kelvin-Helmholtz-Darcy theory, we develop the gap-averaged Navier-Stokes equations and end up with the stable standing waves with half frequency of the external forced vibration. To overcome the dependency of a numerical model on the experimental parameter of wave length, we take two-phase flow into consideration and a novel dispersion relation is derived. The numerical results compare well with our experimental data, which effectively validates our proposed mathematical model. Therefore, this model can produce robust solutions of Faraday wave patterns and resolve related physical phenomena, which demonstrates the practical importance of the present study. *Published by AIP Publishing.* <https://doi.org/10.1063/1.5022424>

I. INTRODUCTION

Faraday waves arise in a vertically vibrating container filled with liquids. In 1831, Faraday carried out experiments and for the first time noticed that the frequency of the wave motions was half that of the external vibrations.¹ Matthiessen² and Rayleigh³ studied the waves experimentally but obtained different results that the vibration was synchronous by the former and, however, half-frequency by the latter. The distinction then was explained by Benjamin and Ursell via the theory of Mathieu functions which give solutions of several instability regions corresponding to different responses.⁴ This work shed light on the theoretical analysis and motivated more researchers thereafter to explore the untapped knowledge on Faraday waves. Miles and Henderson reviewed the studies of great physical significance, especially for those of stability and bifurcation in terms of different resonances.⁵

Among the properties of Faraday waves, the diverse wave patterns have attracted the most attention due to the complexity in the presence of nonlinearity, and it is easy to investigate such an important issue by relatively simple experimental devices. Wave patterns observed in experiments include squares, hexagons,⁶ stripes, stars,⁷ and lattice.⁸ Recently, in a Hele-Shaw cell, a new type of standing wave which is steep and solitary like was found under periodic oscillations.⁹ This research inspired Li *et al.* to conduct experiments in a Hele-Shaw cell filled with water-ethanol solution.¹⁰ A combined structure was discovered such that three types of localized standing waves can be connected following a combination law. Another new family of waves was found in the Hele-Shaw cell which was filled in pure ethanol but with extremely shallow liquid depth.¹¹ Although these experiments provide a new perspective and enrich the knowledge of Faraday waves, the mechanism of these wave patterns is less well understood. It becomes quite essential to develop a reliable theory to

explain. For this matter, Perinet *et al.* numerically investigated the subcritical bifurcation of Faraday waves at the interface between two immiscible incompressible liquids,¹² in which the computational results seem quite close to the standing waves observed by Li *et al.*¹¹ Ignoring the effect of internal wall attenuation leads to a simplified model, which, however, is not appropriate to deal with narrow tanks like the Hele-Shaw cell. Ubal *et al.* also studied two-dimensional Faraday waves by means of numerical simulation¹³ and compared the computational results with theoretical solutions of instability regions.^{4,14} Although the free surface given by Ubal *et al.* displays a similar wave profile¹³ to what was described by Li *et al.*,¹¹ their numerical study was carried out by simply solving two-dimensional Navier-Stokes equations, which is not sufficient to recover the three-dimensional nature of Faraday waves particularly for the viscous effect in the boundary layer.

Considering the three-dimensional Direct Numerical Simulation (DNS), the first difficulty that comes to mind is the high computational cost. Since the width direction in a Hele-Shaw cell is small already, the grid cell size has to be specified much smaller—by six orders of magnitude for Systeme International (SI) units—so as to exactly capture the shear dissipation within the thin boundary layer. The computational cost increases rapidly and soon exceeds the maximum capability of modern architecture. Seeking a more accurate yet efficient approach for resolving the related fluid dynamics, some mathematical model derivation has been attempted. Due to the confined fluid between two vertical walls, early scientists used Darcy's law to treat it through a porous medium. It thus permits visualization of this fluid motion in two dimensions. This model works well if the inertial forces are negligible in comparison to the viscous effect.¹⁵ For the circumstance that the inertial forces are significant, a new model, namely, the Kelvin-Helmholtz-Darcy theory, was proposed by Gondret and Rabaud to address the shear instability of two-fluid parallel flow in a Hele-Shaw cell.¹⁶ They merged the transverse

^{a)}Electronic mail: sjliao@sjtu.edu.cn

dissipation and two-dimensional Navier-Stokes equations into a mixing of Euler and Darcy equations, which was used to analyze the linear instability of the two-fluid parallel flow.^{16,17} More recently, Talib *et al.* modified this model by including periodic forces to compute the wave instability in a horizontal oscillatory Hele-Shaw cell.¹⁸ It is noted that detailed wave profiles were not involved in all the above studies which are a vital characteristic of Faraday waves. Therefore, we establish a novel model, the gap-averaged Navier-Stokes equations based on the Kelvin-Helmholtz-Darcy theory, and validate it by a series of laboratory experiments.

Another issue related to the robust computation is how to determine the wave length on which our numerical model highly depends. It gives rise to the dispersion relation for the estimation of wave length in practice. The most widely applied one was proposed by Benjamin and Ursell.⁴ However, Rajchenbach and Clamond suggested that “the possible wavenumbers of resonating Faraday waves are not quantised by the container” and also pointed out that the dispersion relation that people often used is actually the one of free unforced surface waves, and the misuse has led to many miscalculations of the wavenumber as well as incorrect physical interpretations.¹⁹ Starting from single phase flow, Rajchenbach *et al.* derived the weakly nonlinear dispersion relation for parametrically forced water waves in a Hele-Shaw cell.⁹ Unfortunately, only the linear relation is available due to the unknown wave amplitude. Here, it is worth mentioning that despite their creative and inspiring work, there is no validation or verification provided for the newly derived relation. In this work, we modify the dispersion relation which takes air into consideration by solving the Mathieu form equation via a combined approach and validate it with our numerical results.

The first aim of this paper is to develop an appropriate mathematical model to describe the flow motion of the Faraday waves in Hele-Shaw cells. As shown below, the proposed model is validated well and shows good agreement with the experimental results. The second aim of this paper is to establish a rational dispersion relation that can provide a reliable estimation of wave length for the numerical computation. The resultant numerical model augmented with the dispersion relation can then produce a robust solution of standing waves in a Hele-Shaw cell.

The paper is organized as follows. In Sec. II, we describe the configuration of the laboratory experiments. In Sec. III, we introduce how we get the gap-averaged Navier-Stokes equations from the Poiseuille type assumption. Then we explain the numerical setup in Sec. IV to solve the previous equations in Hele-Shaw cells, followed by the dispersion relation derived in Sec. V. Finally, we show the laboratory data and the numerical solutions in Sec. VI, in which details involving non-dimensional analysis and comparison of dispersion relations are reported as well.

II. EXPERIMENTAL SETUP

Figure 1 shows the schematic of the experimental setup. We use the absolute ethanol at a temperature of approximately 25 °C as the working liquid in our laboratory experiments. The Hele-Shaw cell is a container made of polymethyl

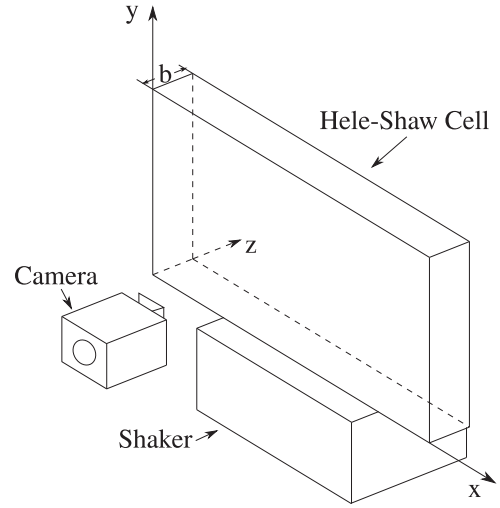


FIG. 1. Device schematic of experimental setup. b denotes the gap size.

methacrylate (PMMA) with 300 mm long, 60 mm depth, and 1.7 mm width (the gap size), which is fixed on a shaker and made to oscillate vertically with sinusoidal motion. The top gap of the container is covered by a lid and sealed due to the volatilization of ethanol. The amplitude of the acceleration is observed by using an oscilloscope through an amplifier connecting a piezoelectric sensor which is used to gauge the acceleration of the shaker by converting it to an electrical charge. By reading the concrete values from the oscilloscope, we adjust the output voltage from the amplifier. Before we conduct any experiments, we ensure that the floor is flat by using a level meter. On top of that, the shaker is very heavy (95 kg) and it was directly put on the flat floor. Given the shaker’s fundamental frequency of 8000 Hz, the torquing motion is largely prevented by the experimental frequency less than 30 Hz. Its make and model is ESS-050. All the free surface patterns are recorded by using a high-speed (400 fps) camera which is oriented perpendicular to the front wall of the Hele-Shaw cell. In our experiment, the liquid depth and the oscillatory frequency are varied.

III. GAP-AVERAGED NAVIER-STOKES EQUATIONS

Now we consider a Hele-Shaw cell filled with viscous fluids under gravity, which is governed by incompressible Navier-Stokes equations. Since the width b of tank is quite thin, it is classical to assume that the flow in the z direction is of Poiseuille type. The velocity profile is supposed to remain a parabolic shape in z . We have the following definition

$$u'(x, y, z) = \frac{3}{2} \left(1 - \left(\frac{z}{b/2} \right)^2 \right) u(x, y), \quad (1)$$

$$v'(x, y, z) = \frac{3}{2} \left(1 - \left(\frac{z}{b/2} \right)^2 \right) v(x, y), \quad (2)$$

$$w' = 0, \quad (3)$$

where u , v , and w with a prime are the components of gap-averaged velocities in x , y , and z directions, respectively. Using the assumption of (1)–(3), three-dimensional Navier-Stokes

equations are integrated across the gap. By averaging them, we can obtain a simplified two-dimensional system¹⁶

$$\frac{\partial u}{\partial x} + \frac{\partial v}{\partial y} = 0, \quad (4)$$

$$\frac{\partial u}{\partial t} + \alpha \left(u \frac{\partial u}{\partial x} + v \frac{\partial u}{\partial y} \right) = -\frac{1}{\rho} \frac{\partial p}{\partial x} + \nu \beta \left(\frac{\partial^2 u}{\partial x^2} + \frac{\partial^2 u}{\partial y^2} \right) - \frac{12\nu}{b^2} u, \quad (5)$$

$$\frac{\partial v}{\partial t} + \alpha \left(u \frac{\partial v}{\partial x} + v \frac{\partial v}{\partial y} \right) = -\frac{1}{\rho} \frac{\partial p}{\partial y} + \nu \beta \left(\frac{\partial^2 v}{\partial x^2} + \frac{\partial^2 v}{\partial y^2} \right) - \frac{12\nu}{b^2} v - g, \quad (6)$$

where p , ρ , ν , and g denote pressure, density, kinetic viscosity, and gravity, respectively. Since the prefactors α and β are derived as 6/5 and 0, respectively, the viscous term is believed to be negligible,¹⁶ which is also adopted in analysis of Faraday waves,⁹ but an alternative set of $\alpha = 54/35$ and $\beta = 6/5$ is suggested in another study.²⁰

In our research, the viscous effect due to shear flow is taken into account, particularly in the vicinity of the bottom boundary and of the free surface. Thus we include the viscous term combining with gravity and capillary force to develop the so-called gap-averaged Navier-Stokes equations

$$\frac{\partial u}{\partial x} + \frac{\partial v}{\partial y} = 0, \quad (7)$$

$$\frac{\partial u}{\partial t} + \frac{6}{5} \left(u \frac{\partial u}{\partial x} + v \frac{\partial u}{\partial y} \right) = -\frac{1}{\rho} \frac{\partial p}{\partial x} + \nu \left(\frac{\partial^2 u}{\partial x^2} + \frac{\partial^2 u}{\partial y^2} \right) - \frac{12\nu}{b^2} u + \frac{1}{\rho} T_x, \quad (8)$$

$$\frac{\partial v}{\partial t} + \frac{6}{5} \left(u \frac{\partial v}{\partial x} + v \frac{\partial v}{\partial y} \right) = -\frac{1}{\rho} \frac{\partial p}{\partial y} + \nu \left(\frac{\partial^2 v}{\partial x^2} + \frac{\partial^2 v}{\partial y^2} \right) - \frac{12\nu}{b^2} v - \tilde{g} + \frac{1}{\rho} T_y, \quad (9)$$

where $\tilde{g} = g - F \cos \omega t$ with F the acceleration amplitude and ω is the oscillatory angular frequency. T_x and T_y represent the components of surface tension \mathbf{T} in x and y directions, respectively, where \mathbf{T} is given as²¹

$$\mathbf{T} = \sigma \kappa \delta_S \mathbf{n}. \quad (10)$$

The notation σ denotes the surface tension coefficient, κ the free surface curvature, δ_S the Dirac distribution function of the interface, and \mathbf{n} the unit normal of the interface. Since the real shape of the interface in the Hele-Shaw cell is not known in prior, the three-dimensional effect needs to be taken into account in the surface tension approximation. Although a more sophisticated option is provided,¹⁵ in this study, we prefer to use an empirical coefficient σ for the sake of simplicity.

IV. NUMERICS

Gap-averaged Navier-Stokes equations (7)–(9) are implemented and solved directly using an open source code Gerris,^{22,23} where some sophisticated techniques are integrated to improve the solution quality. The advanced piecewise

linear interface calculation (PLIC) scheme is used for the volume of fluid (VOF) method to capture the moving interface and the height function which is employed for precise approximation of curvature in surface tension calculation. Moreover, it allows an octree adaptive refinement strategy for the region in the presence of the large gradient of VOF function. With all the efforts mentioned above, this code is highly appealing in our numerical simulation which has also been verified well and validated by numerous applications.^{24–27}

If we define the characteristic length $L = Ub^2/(12\nu)$ and the characteristic velocity $U = F/f$ with f being $\omega/(2\pi)$, we can obtain $x = \alpha L \bar{x}$, $y = \alpha L \bar{y}$, $u = U \bar{u}$, $v = U \bar{v}$, $t = L \bar{t}/U$, $p = \alpha \rho_1 U^2 \bar{p}$, $\tilde{g} = U^2 \bar{g}/L$, and $\sigma = \rho_1 U^2 \bar{\sigma}$. To develop the mathematical model inside the Gerris code, we write gap-averaged Navier-Stokes equations in non-dimensional forms

$$\frac{\partial \bar{u}}{\partial \bar{x}} + \frac{\partial \bar{v}}{\partial \bar{y}} = 0, \quad (11)$$

$$\frac{\partial \bar{u}}{\partial \bar{t}} + \left(\bar{u} \frac{\partial \bar{u}}{\partial \bar{x}} + \bar{v} \frac{\partial \bar{u}}{\partial \bar{y}} \right) = -\frac{\rho_1}{\rho} \frac{\partial \bar{p}}{\partial \bar{x}} + \frac{1}{Re} \left(\frac{\partial^2 \bar{u}}{\partial \bar{x}^2} + \frac{\partial^2 \bar{u}}{\partial \bar{y}^2} \right) - \frac{\nu}{\nu_1} \bar{u} + \frac{\rho_1}{\rho} \bar{T}_x, \quad (12)$$

$$\frac{\partial \bar{v}}{\partial \bar{t}} + \left(\bar{u} \frac{\partial \bar{v}}{\partial \bar{x}} + \bar{v} \frac{\partial \bar{v}}{\partial \bar{y}} \right) = -\frac{\rho_1}{\rho} \frac{\partial \bar{p}}{\partial \bar{y}} + \frac{1}{Re} \left(\frac{\partial^2 \bar{v}}{\partial \bar{x}^2} + \frac{\partial^2 \bar{v}}{\partial \bar{y}^2} \right) - \frac{\nu}{\nu_1} \bar{v} - \bar{g} + \frac{\rho_1}{\rho} \bar{T}_y, \quad (13)$$

where $Re = \alpha^2 LU/\nu$. It is noted that the subscript 1 denotes the main liquid, namely, the pure ethanol in our experiment. Variables without any subscript denote the fluid property determined by the given VOF function.

To reproduce the periodic wave pattern, we consider the computational domain consisting of six crests and troughs with periodic boundary conditions, as shown in Fig. 2. The bottom and the top boundaries are specified with non-slip and symmetric (slip wall) boundary conditions, respectively. Since the Gerris code can only use the quad/octree structure for grid addressing, we divide the domain into two computational boxes and partition each box with Cartesian grids refined by the rule of 2^{level} , where the superscript *level* denotes the level of refinement.²² For the adaptive grids, the maximum value of *level* varies between 6 and 7 to provide convergent solution since the periodic wave pattern is “highly sensitive to viscous damping.”²⁸ Moreover the maximum time step is

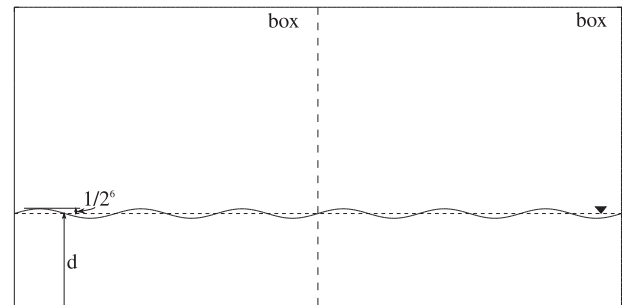


FIG. 2. Configuration of computational condition. d denotes the liquid depth. $1/2^6$ is the amplitude of the initial perturbation.

TABLE I. Physical parameters.

	Liquid	Air
Density (kg/m ³)	791	1.225
Dynamic viscosity (kg/ms)	1.096 × 10 ⁻³	1.789 × 10 ⁻⁵

5 × 10⁻³ with the default Courant-Friedricks-Lewey (CFL) number. The adaptive strategy depends on the norm of the local gradient of the filtered VOF function, and the maximum cell cost allowed is up to 1 × 10⁻³. Despite the existence of numerical sensitivity, most of our cases can obtain consistent results after the use of particular refinement strategy. The initial free surface is the flat state plus a sinusoidal wave perturbation whose amplitude is as same as the size of one grid cell for *level* = 6. The initial wavenumber corresponding to the wave length plays a critical role in determining the robust wave mode excited by the certain vibration, which will be further explored in Sec. V. The physical parameters of the two fluids are given in Table I.

V. DISPERSION RELATION

Rajchenbach and Clamond pointed out that the possible wave length of Faraday waves has nothing to do with the container.¹⁹ This conclusion agrees well with our observation that the main wave profile varies as the external force changes, which means that the natural frequency of the fluid in a certain tank hardly affects the major resonating modes. However, the wave elevation is always observed at either crest or trough in the vicinity of the lateral walls. This finding implies that some waves are squeezed or spread, which largely increases the numerical complexity. This effect of contact lines has been reported in several studies.^{4,29,30} Therefore, a feasible dispersion relation is included in practice to provide a more precise wave length approximation. Distinguished from Rajchenbach and Clamond who proposed a linear dispersion relation in the single phase flow,¹⁹ we derive a more reliable relation that takes two-phase flow into consideration. The techniques we use to derive Mathieu equation here are widely applied to Faraday waves.^{4,14}

Starting from Eqs. (7)–(9), gap-averaged Navier-Stokes equations are simplified by neglecting the viscous term as well as the capillary force term, which yields

$$\frac{\partial u_j}{\partial x} + \frac{\partial v_j}{\partial y} = 0, \quad (14)$$

$$\frac{\partial u_j}{\partial t} + \alpha \left(u_j \frac{\partial u_j}{\partial x} + v_j \frac{\partial u_j}{\partial y} \right) = -\frac{\partial p_j}{\rho_j \partial x} - \gamma_j u_j, \quad (15)$$

$$\frac{\partial v_j}{\partial t} + \alpha \left(u_j \frac{\partial v_j}{\partial x} + v_j \frac{\partial v_j}{\partial y} \right) = -\frac{\partial p_j}{\rho_j \partial y} - \tilde{g} - \gamma_j v_j, \quad (16)$$

$$\gamma_j = \frac{12\nu_j}{b^2}, \quad (17)$$

where subscript *j* denotes different phase of fluids. Following Rajchenbach *et al.*,⁹ we assume that the two-dimensional flow is vortex free and hence a velocity potential meets $\partial_x \phi = u$ and $\partial_y \phi = v$. We can rewrite previous Eqs. (15) and (16) in terms

of velocity potential ϕ by integrating along the streamline as

$$\frac{\partial \phi_j}{\partial t} + \gamma_j \phi_j + \frac{\alpha}{2} (\nabla \phi_j)^2 + \frac{p_j}{\rho_j} + \tilde{g}y = 0. \quad (18)$$

Since the free surface tension is neglected where $p_1 - p_2 = 0$ holds at the fluid interface, we can obtain

$$\begin{aligned} \frac{\partial}{\partial t} (\rho_1 \phi_1 - \rho_2 \phi_2) + (\rho_1 \gamma_1 \phi_1 - \rho_2 \gamma_2 \phi_2) + (\rho_1 - \rho_2) \tilde{g}y = 0 \\ \text{at } y = \eta(x, t), \end{aligned} \quad (19)$$

by linear approximation with $\eta(x, t)$ being the function of free surface elevation. Since no fluid can pass through the bottom, we include the impenetrable boundary condition and the infinite boundary condition for the top

$$\frac{\partial \phi_1}{\partial y} = 0 \quad \text{at } y = d, \quad (20)$$

$$\frac{\partial \phi_2}{\partial y} = 0 \quad \text{at } y = +\infty, \quad (21)$$

for the lower and the upper layer of fluids, respectively. At the vicinity of the interface, we also include

$$\frac{\partial \eta}{\partial t} = \frac{\partial \phi_j}{\partial y} \quad \text{at } y = \eta(x, t) \quad (22)$$

to consider the kinetic boundary condition of the free surface. Supposing $\eta = \bar{\eta} e^{ikx}$, we can obtain the solutions of Laplace equation of ϕ_j

$$\phi_j = \bar{\phi}_j(y, t) e^{ikx}, \quad (23)$$

$$\bar{\phi}_1 = \frac{d\bar{\eta} \cosh kd + y}{kdt \sinh kd}, \quad (24)$$

$$\bar{\phi}_2 = -\frac{d\bar{\eta}}{kdt} e^{-ky}. \quad (25)$$

Substituting (23) into (19), we then derive the damped Mathieu equation

$$\frac{d^2 \bar{\eta}}{dt^2} + \frac{\rho_1 \gamma_1 \coth kd + \rho_2 \gamma_2}{\rho_1 \coth kd + \rho_2} \frac{d\bar{\eta}}{dt} + \frac{k(\rho_1 - \rho_2)}{\rho_1 \coth kd + \rho_2} \tilde{g} \bar{\eta} = 0, \quad (26)$$

and obtain the no-damping and no-forcing linear wave dispersion relation as

$$\Omega^2 = \frac{k(\rho_1 - \rho_2)g}{\rho_1 \coth kd + \rho_2}, \quad (27)$$

where Ω is the angular frequency of the response. For the sake of brevity, let us define

$$A = \frac{\rho_1 \gamma_1 \coth kd + \rho_2 \gamma_2}{\rho_1 \coth kd + \rho_2}, \quad (28)$$

$$B = \frac{k(\rho_1 - \rho_2)}{\rho_1 \coth kd + \rho_2}, \quad (29)$$

$$\bar{\eta} = \zeta e^{\int -\frac{A}{2} dt} = \zeta e^{-\frac{At}{2}}. \quad (30)$$

We finally obtain the Mathieu form equation from Eq. (26)

$$\frac{d^2 \zeta}{dT^2} + (p - 2q \cos 2T)\zeta = 0, \quad (31)$$

$$p = \frac{4Bg - A^2}{\omega^2}, \quad (32)$$

$$q = \frac{2Bf}{\omega^2}, \quad (33)$$

provided that $T = 1/(2\omega t)$. Many researchers employed Floquet-based analysis to analyze the linear instability of Faraday waves.^{13,14,31} According to this technique, the solutions of Mathieu equation (31) are expressed in the form of

$$\zeta(t) = e^{i\mu T} \sum_{l=-n}^n c_l e^{i2lT}. \quad (34)$$

The periodic solutions of (26) are the interest of research, so accordingly we concern the aperiodic solutions of (31). Due to the well-known resonance conditions

$$m\omega = 2\Omega, \quad (35)$$

the Floquet exponent μ is explicitly solved by using

$$\mu = m - i\frac{A}{\omega}, \quad (36)$$

which is the transcendent and implicit dispersion relation. For this matter, we substitute (34) into Eq. (31) by using the approach proposed by Acar and Feeny³² to obtain the l th equation

$$[p - (\mu + 2l)^2] c_l - qc_{l-1} - qc_{l+1} = 0. \quad (37)$$

The linear equation system (37) can also be expressed in the matrix form

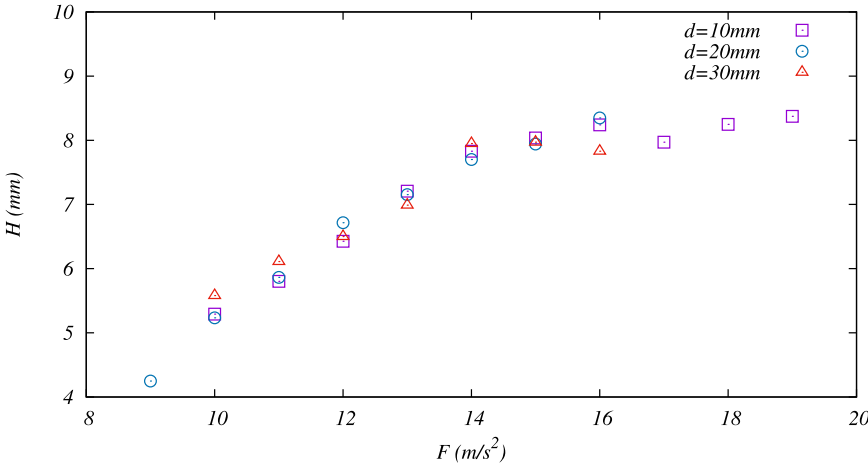
$$\mathbf{K}\mathbf{c} = \begin{bmatrix} k_{-n} & -q & 0 & 0 & 0 \\ -q & \ddots & -q & 0 & 0 \\ 0 & -q & k_0 & \ddots & 0 \\ 0 & 0 & \ddots & \ddots & -q \\ 0 & 0 & 0 & -q & k_n \end{bmatrix} \begin{pmatrix} c_{-n} \\ \vdots \\ c_0 \\ \vdots \\ c_n \end{pmatrix} = \begin{pmatrix} 0 \\ \vdots \\ 0 \\ \vdots \\ 0 \end{pmatrix}, \quad (38)$$

where $k_l = p - (\mu + 2l)^2$. To gain nontrivial solutions of vector \mathbf{c} , the determinant of \mathbf{K} has to be zero. Thus we solve

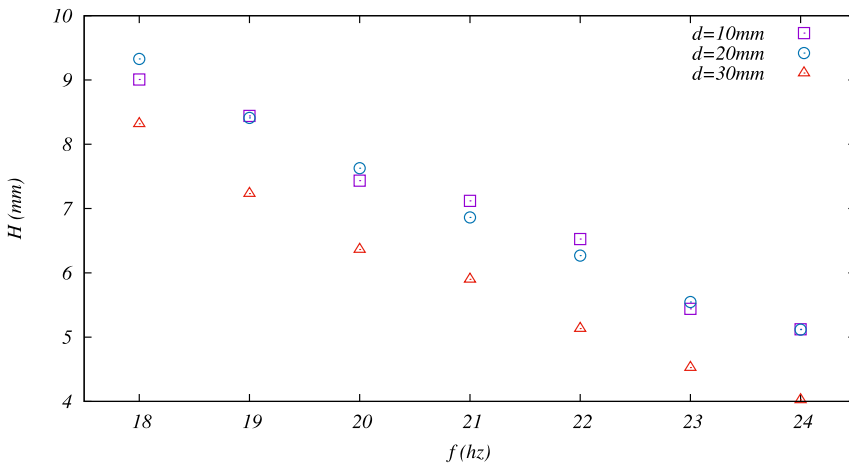
$$\det(\mathbf{K}) = 0, \quad (39)$$

with given μ (36) and $n = 2$ which was suggested by Acar and Feeny³² to be adequate for convergent solutions.

We use an iterative method in *Mathematica* to obtain the value of wavenumber k . Note that the real part of k is the spatial



(a)



(b)

FIG. 3. All average wave heights measured in laboratory experiments. (a) Dot plot against forcing acceleration; (b) dot plot against forcing frequency.

wavenumber and the imaginary part is the spatial growth rate (negative) or the significance of decaying behavior (positive).

VI. RESULTS AND DISCUSSIONS

A. Laboratory data

The pattern of Faraday waves is thoroughly investigated under various experimental conditions, namely, liquid depth

(d), acceleration amplitude (F), and forcing frequency (f). To alleviate measurement errors, we gauge wave lengths and wave heights five times for each condition, which are elaborated in Tables II and III (see the Appendix). To give an intuitive impression on the experimental data, we draw the wave height with respect to F and f in Fig. 3. It is shown that the results of wave height are closely related to the condition of the amplitude and the frequency. More concretely, the wave height increases nearly linearly with regard to F and finally

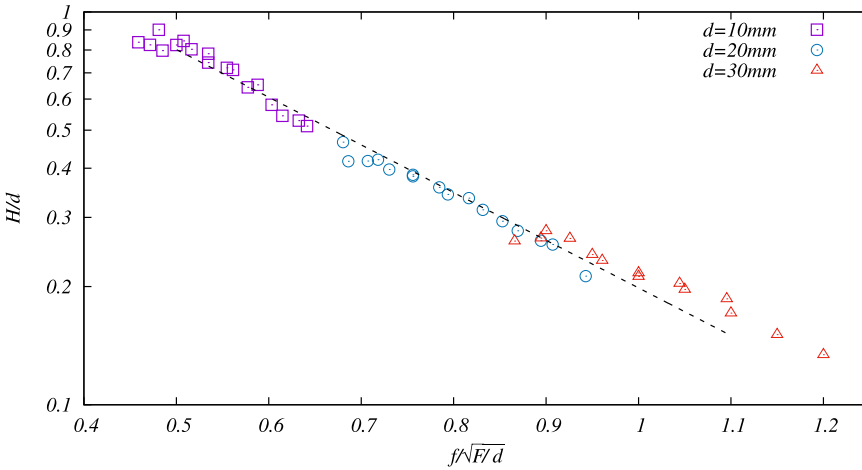


FIG. 4. The dot plot of average experimental data from Fig. 3 after nondimensionalization. The dashed line is the fitting function $\log\left(\frac{H}{d}\right) \approx -1.21 \frac{f}{\sqrt{F/d}} + 0.51$.

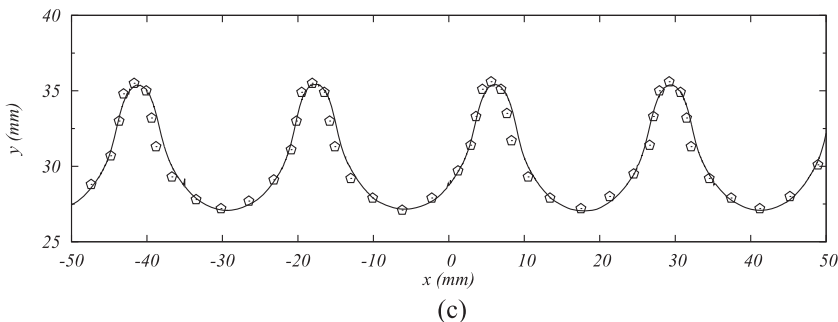
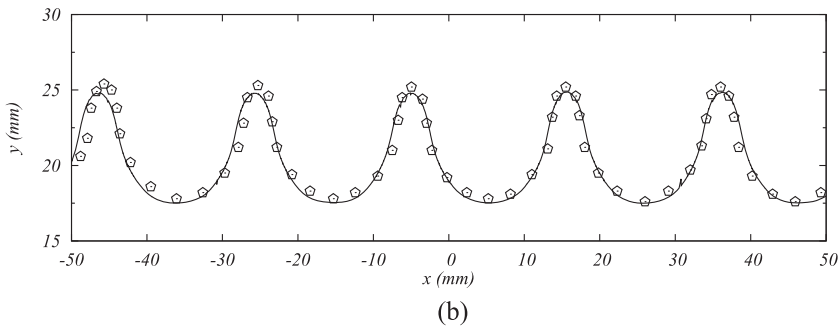
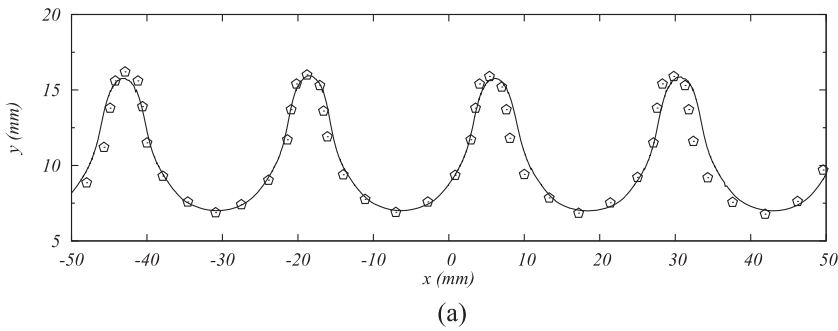


FIG. 5. The highest computational wave profiles (solid lines) against the experimental data (pentagons). (a) The case with $d = 10$ mm, $f = 18$ Hz, and $F = 14$ m/s²; (b) the case with $d = 20$ mm, $f = 20$ Hz, and $F = 14$ m/s²; (c) the case with $d = 30$ mm, $f = 18$ Hz, and $F = 12$ m/s².

stabilizes around 8 mm at $f = 20$ Hz. In contrast, the wave height decreases linearly when F is fixed but f varies. This observation is in accordance with our common understanding that more violent resonance is expected at higher external force or lower temporal frequency. It is noted that the wave height hovers once F arrives at 16 m/s^2 which may be the critical value of forming robust standing wave. Nevertheless, the effect of liquid depth d is less significant where the differences of H are unnoticeable, as shown in Fig. 3.

In addition to the above qualitative evaluation, we give a more clear description to relate wave height with liquid depth, acceleration amplitude, and forcing frequency for Faraday waves in Hele-Shaw cells. For stable standing waves, the wave height is parameterized in this problem as

$$H = H(f, F, d), \quad (40)$$

which, due to two independent physical dimensions, can be written in a non-dimensional form as

$$\frac{H}{d} = \Pi\left(\frac{f}{\sqrt{F/d}}\right). \quad (41)$$

Now it is easier to understand the essential relation behind the raw experimental data. But what is the exact expression of the function Π ? To answer this question, we first plot (41) as shown in Fig. 4 which can be approximated by a logarithmic

expression as

$$\log\left(\frac{H}{d}\right) \approx -1.21 \frac{f}{\sqrt{F/d}} + 0.51. \quad (42)$$

The constants appearing in (42) probably vary with distinct physical parameters, including the fluid density, the viscosity, and the gap between the vertical walls of the Hele-Shaw cell.

B. Numerical analysis

The numerical simulation is carried out following the solution procedure described in Sec. IV, provided that the wave length is determined by averaging experimental data, as shown in Tables II and III. We choose the cases with strong nonlinear effect which is very challenging for numerical simulation. It is found that the computed frequency of response is just half of the forcing frequency, which compares favorably with our experimental observation. We have also plotted the wave profiles in Fig. 5 which shows excellent agreement with the free surface obtained in our experiments. Such a comparison has never been reported in the previous literature, which demonstrates that gap-averaged Navier-Stokes equations (7)–(9) can be viewed as a proper mathematical model for Faraday waves in Hele-Shaw cells.

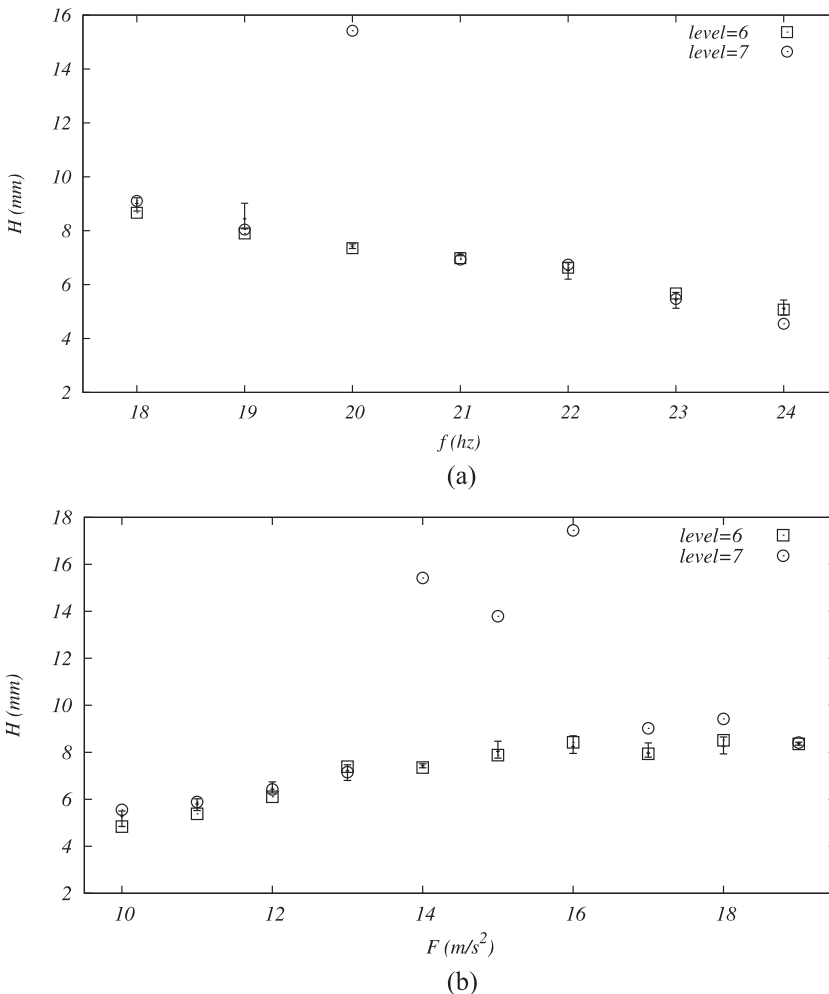
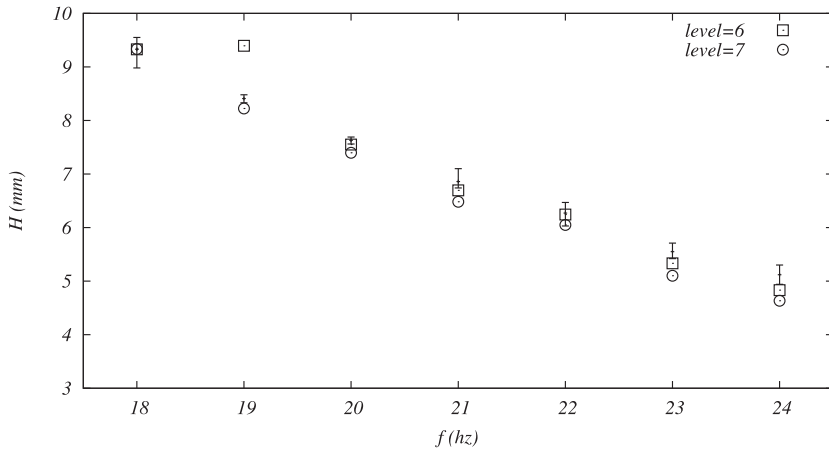


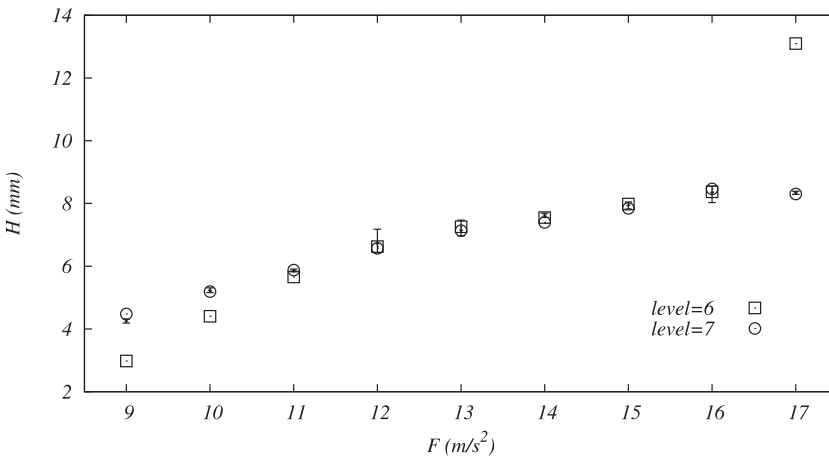
FIG. 6. The computational wave heights when $d = 10$ mm for different mesh refinements. Squares: wave heights computed with mesh level = 6; circles: wave heights computed with mesh level = 7; error bars: wave heights gauged in laboratory experiments. (a) Dot plot against forcing frequency with $F = 14 \text{ m/s}^2$; (b) dot plot against forcing acceleration with $f = 20$ Hz.

Quantitatively, we plot the numerical solution under different grid resolutions. Since the wave profile may not be uniform or periodic, we measure the wave height by using the largest values between troughs and crests of wave elevation. The results are depicted with regard to the forcing frequency and the acceleration amplitude in Figs. 6–8 in order of the liquid depth d . In Fig. 6, it is found that the computed wave heights show an overall good agreement with experimental measurements and the ones with mesh $level = 6$ are more superior.

If we look back at Fig. 4, we can realize that the shallower liquid depth corresponds to larger H/d value, which indicates more violent motion of the free surface. As mentioned by Bouchgl *et al.*, the simulation of fluid in oscillatory Hele-Shaw cells is very sensitive to viscous damping²⁸ such that even tiny change of dissipation may influence the wave modes. Thus the closer agreement for coarser grid in the shallow water condition can be explained by that more dissipation is required for robust calculation of nonlinearity. The sensitivity of numerical



(a)



(b)

FIG. 7. The computational wave heights when $d = 20$ mm for different mesh refinements. Squares: wave heights computed with mesh $level = 6$; circles: wave heights computed with mesh $level = 7$; error bars: wave heights gauged in laboratory experiments. (a) Dot plot against forcing frequency with $F = 14$ m/s²; (b) dot plot against forcing acceleration with $f = 20$ Hz.

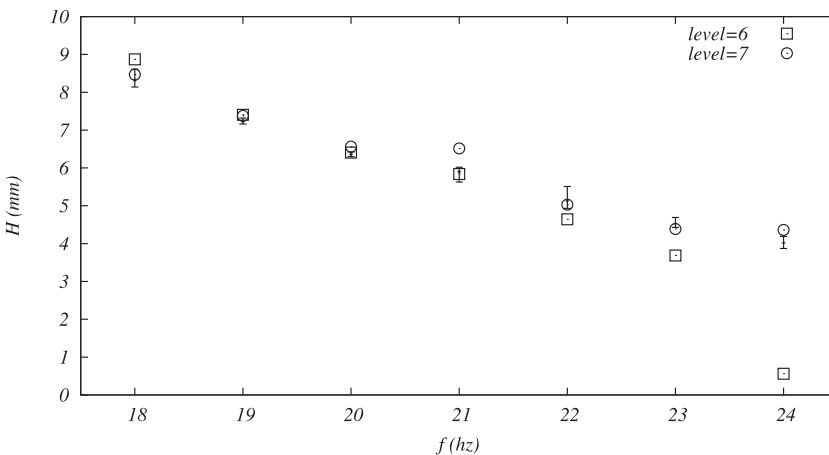


FIG. 8. The computational wave heights against forcing frequency with $F = 12$ m/s² when $d = 30$ mm for different mesh refinements. Squares: wave heights computed with mesh $level = 6$; circles: wave heights computed with mesh $level = 7$; error bars: wave heights gauged in laboratory experiments.

results on computational mesh also indicates that it may turn into other wave modes with higher wavenumbers due to the instability. In contrast, the numerical results computed with other two liquid depths barely experience distinct discrepancy for different grid resolutions. As shown in Figs. 7 and 8, nearly all numerical results coincide with the normal range of experimental data and the ones with $level = 7$ seem to have higher solution accuracy. The complete analysis gives us an intuitive image to understand how the liquid depth or the motion of fluid in this problem may bring challenges for the numerical computation. Moreover, it is hard to find any laws ruling this mode bifurcation due to its irregular distribution which is also beyond the interest of the present study. As shown above, the developed gap-averaged Navier-Stokes equations (7)–(9) are verified as a reliable numerical model to simulate Faraday waves in Hele-Shaw cells.

Now we have the access to the flow information which cannot be conveniently obtained by experimental means. The vorticity maps and the velocity vectors of Faraday waves during T_0 one cycle of external vibration are demonstrated in Fig. 9.

C. Analysis on dispersion relation

So far, an accurate dispersion relation that contains key ingredients to perform simulation has not been well built or validated yet. In addition to the proposed two-phase dispersion relation, we will carry out some comparisons with two alternative dispersion relations. One is the no-damping and no-forcing linear wave dispersion relation⁴

$$\Omega^2 = kg \tanh kd. \quad (43)$$

The other one is the dispersion relation proposed by Rajchenbach *et al.*⁹ which reads as

$$[1 - \omega / (2\omega_0)]^2 = F^2/16 - \gamma^2 / (4\omega_0^2), \quad (44)$$

with γ being $12\nu/b^2$. ω_0 denotes the no-damping and no-forcing angular frequency of linear waves, i.e., $\omega_0^2 = kg \tanh kd$. This relation is thought as the first theoretically correct dispersion relation on Faraday waves in a Hele-Shaw cell. All the above relations will be validated by the present experiment data.

In this study, we focus on the smallest real part of the wavenumber $k = 2\pi/\lambda$, where k is implicit and thus to be calculated numerically. We first present the results with regard to the forcing frequency in Fig. 10 sorted by the liquid depth. At first glance, none of the relations are compared well with experimental data because all current dispersion relations are from linear theory, but most of our cases are strongly nonlinear. The relations probably lose the ability to predict the real nature in this situation. Unfortunately the problem we run into is beyond the existing methods. If we look further, some essential features can be found from the curves. The first point is that the results computed by the present dispersion relation show closer agreement than those by (44). This nature is highly preferred due to the problem's sensitivity. Another point is that the results produced by the new dispersion relation approach the

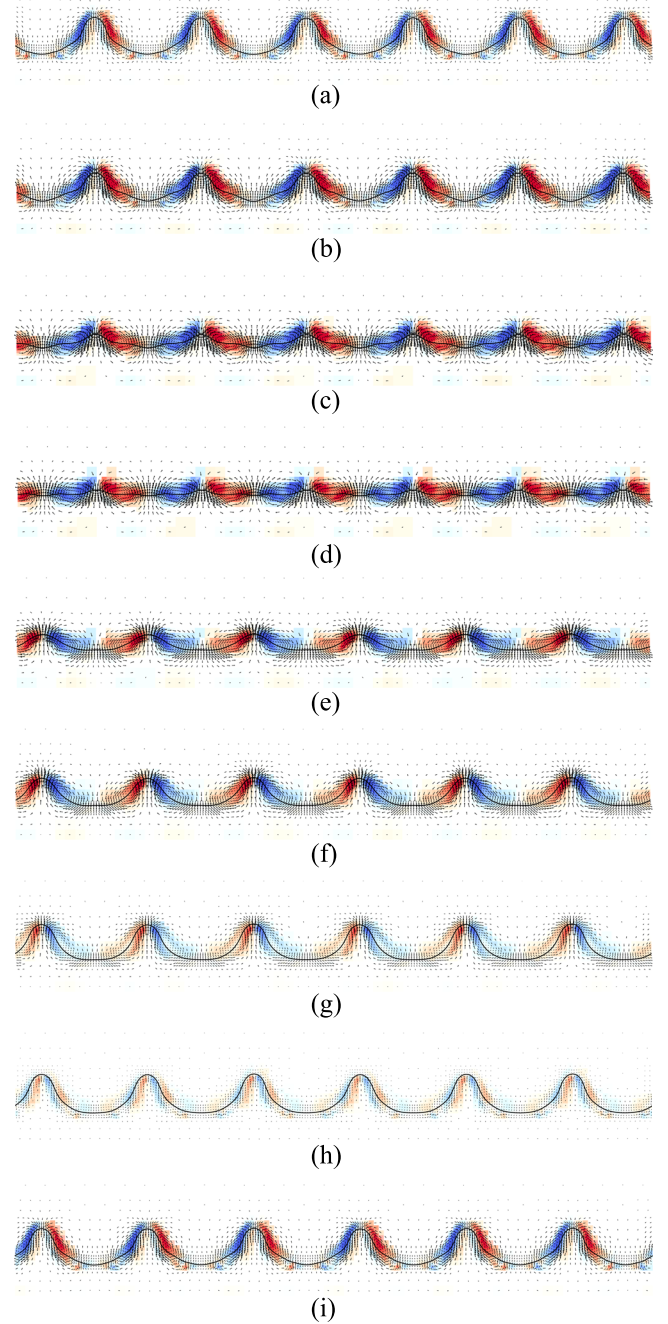


FIG. 9. Snapshots of vorticity contours and velocity vectors during T_0 one cycle of external vibration with $d = 10$ mm, $f = 18$ Hz, and $F = 14$ m/s². The solid arrows represent velocity vectors; the color map represents the amplitude of vorticity field. (a) $t = nT_0$. (b) $t = (n + \frac{1}{8})T_0$. (c) $t = (n + \frac{1}{4})T_0$. (d) $t = (n + \frac{3}{8})T_0$. (e) $t = (n + \frac{1}{2})T_0$. (f) $t = (n + \frac{5}{8})T_0$. (g) $t = (n + \frac{3}{4})T_0$. (h) $t = (n + \frac{7}{8})T_0$. (i) $t = (n + 1)T_0$.

experimental curves as the frequency increases. This finding is of particular importance for the cases of deeper liquid depth d , and it also indicates that the proposed dispersion relation is less suitable for the case with shallower liquid. Although the curves of (43) are closer to the experimental points when forcing frequency is lower, as emphasized before, this relation is misused. As a clearer illustration, since the relation of (43) does nothing with the external force, the profile plotted in

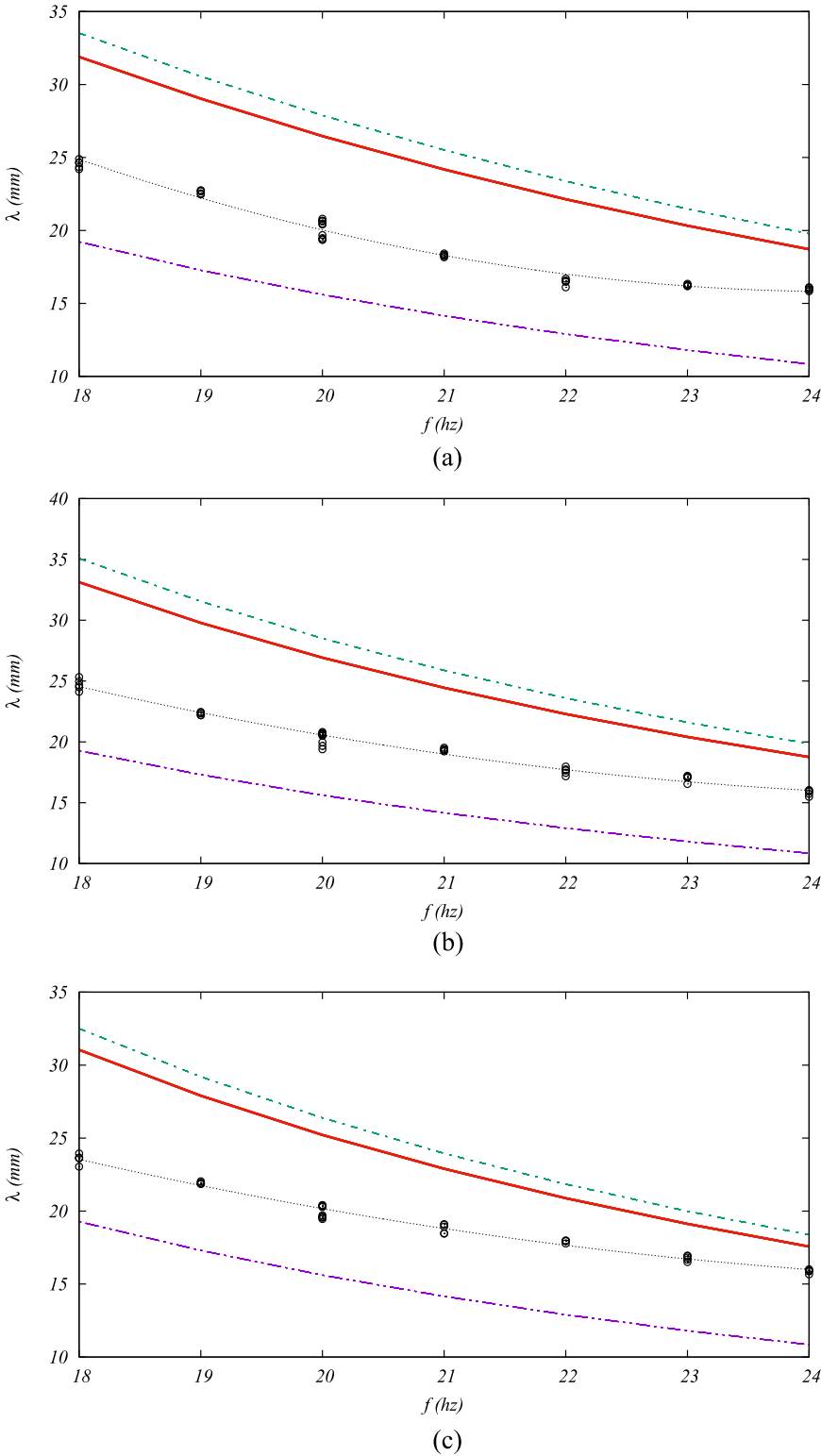
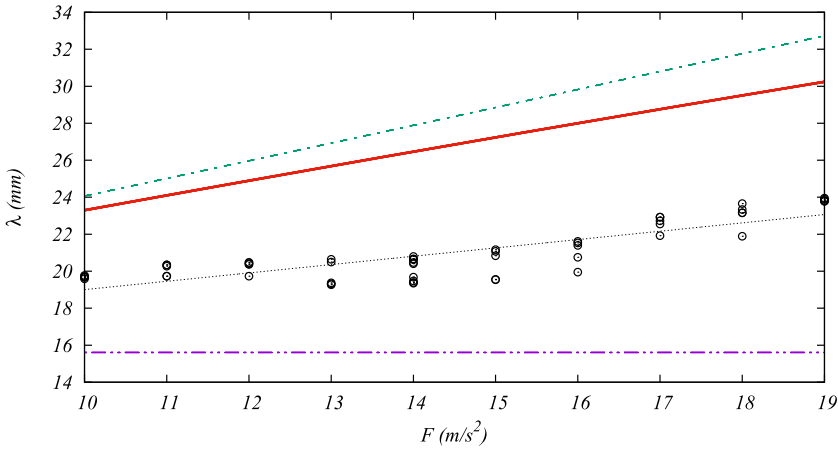


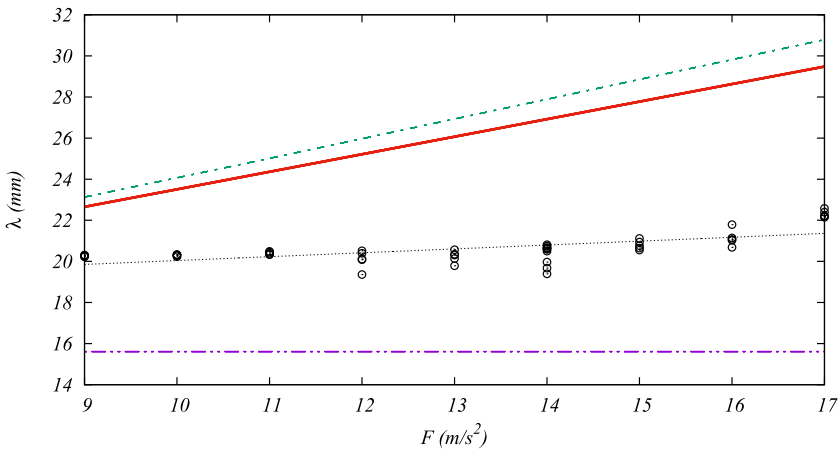
FIG. 10. Dashed lines (---): the dispersion relation for Faraday waves in Hele-Shaw cells by Rajchenbach, Leroux, and Clamond;⁹ dashed lines (-.-.-): the no-damping and no-forcing dispersion relation by Benjamin and Ursell;⁴ circles: experimental data; black dot lines: linear regression fitting experimental data; red solid lines: two-phase flow dispersion relation for Faraday waves in Hele-Shaw cells proposed in this paper. (a) Cases with $d = 10$ mm and $F = 14$ m/s²; (b) cases with $d = 20$ mm and $F = 14$ m/s²; (c) cases with $d = 30$ mm and $F = 12$ m/s².

Fig. 11 is a horizontal line when drawing graph of λ versus F . However, as F increases, the experimental data of λ vary with a distinct rising trend which is reflected by the proposed relation. Similar to Fig. 10, the present curves in Fig. 11 look closer to the experimental results and approach the experimental points as F decreases. The tendency in variation can be explained by the linear theory. Although (44) was originally derived from a weak nonlinear theory, it is reduced into a linear one after

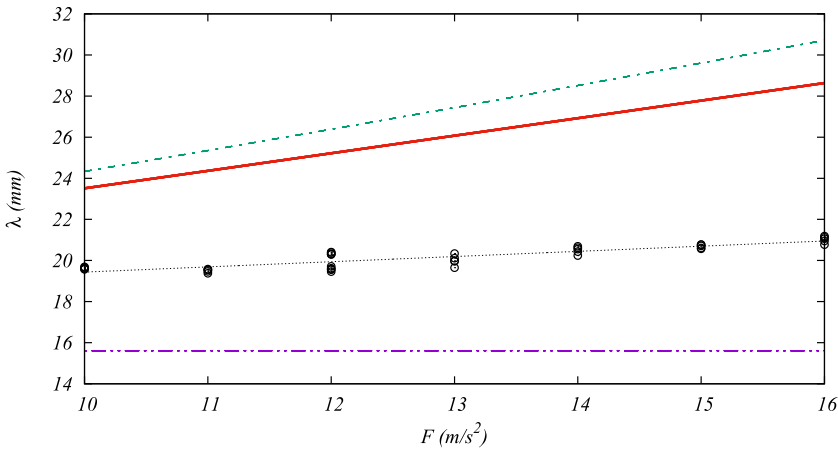
simplification in practical purpose. Thus the two relations fall short of providing adequate capability for resolving nonlinear phenomena emerging in Faraday waves. If we look back at (41), everything makes sense. The dimensionless wave height H/d determines the extent of the nonlinearity. As what we find in Figs. 10 and 11, the dispersion relations for Faraday waves in Hele-Shaw cells behave much better when d is deeper, f is higher, and F is lower. Therefore, as $f/\sqrt{F/d}$ increases and



(a)



(b)



(c)

FIG. 11. Dashed lines (---): the dispersion relation for Faraday waves in Hele-Shaw cells by Rajchenbach, Leroux, and Clamond;⁹ dashed lines (---): the no-damping and no-forcing dispersion relation by Benjamin and Ursell;⁴ circles: experimental data; black dot lines: linear regression fitting experimental data; red solid lines: two-phase flow dispersion relation for Faraday waves in Hele-Shaw cells proposed in this paper. (a) Cases with $d = 10$ mm and $f = 20$ Hz; (b) cases with $d = 20$ mm and $f = 20$ Hz; (c) cases with $d = 30$ mm and $f = 20$ Hz.

H/d lowers down, the dispersion relations work well in this circumstance.

Now we solve the gap-averaged Navier-Stoke equations with wave length provided by the proposed dispersion relation. We perform the simulation for a challenging case with

shallow liquid depth $d = 10$ mm, big forcing frequency $f = 26$ Hz, and relatively small forcing acceleration $F = 4$ m/s². The wave length $\lambda = 10.9553$ mm is determined by the proposed dispersion relation and then is used as a known parameter for numerical simulation. As shown in Fig. 12, a robust



FIG. 12. The computational Faraday wave profile based on the modified dispersion relation with $d = 10$ mm, $f = 26$ Hz, and $F = 4$ m/s².

phenomenon of Faraday waves is reproduced in a Hele-Shaw cell, which well validates the capability of the present model to predict the standing waves at least for some scenarios in which linear phenomenon dominates.

VII. CONCLUSION

Faraday waves in Hele-Shaw cells were mainly studied by using experimental approach.^{9–11,33} It is quite challenging for both theoretical and numerical methods. First, the wave motion is strongly nonlinear, beyond the capability of current theoretical ones. Second, resolving the shear stress in the vicinity of internal walls is significant in Hele-Shaw flow, but it is time-consuming to do three-dimensional numerical simulations. Therefore, since the width direction of Hele-Shaw cells is very small, we first develop the gap-averaged Navier-Stokes equations based on the Kelvin-Helmholtz-Darcy theory which significantly increase the numerical efficiency. To obtain the wave length for determining the computational condition, we derive a novel dispersion relation following Floquet-based analysis which for the first time takes two-phase flow into consideration. We have also carried out experiments in our laboratory.

In this study, we investigate Faraday waves via experimental, numerical, and theoretical studies, particularly for the mechanism of the wave pattern. According to our study, we can make at least the following three significant conclusions. First, by dimensional analysis of the experimental data, we find a logarithmic function to relate wave height with liquid depth, acceleration amplitude, and forcing frequency of

Faraday waves with coefficients determined by the fluid property and the gap size of Hele-Shaw cells. Second, the gap-averaged Navier-Stokes equations are well validated by our laboratory experiments, which has so far not been carried out by anyone else. It is shown that the proposed numerical model overcomes the difficulties of three-dimensional computation and thus demonstrates great practical significance and huge potential to further explore other untapped topics for Faraday waves in Hele-Shaw cells (e.g., bifurcation, cases with shallow liquid depth, multi-phase flow, etc.). Finally, a novel modified dispersion relation based on two-phase flow is developed to predict the wave length for numerical simulations. This relation is compared to be more reliable than other ones available, which can be viewed as an alternative choice in addition to the first theoretically correct dispersion relation by Rajchenbach *et al.*⁹ The proposed gap-averaged Navier-Stokes equations augmented with the new dispersion relation are highly appealing in the further exploration of Faraway waves in Hele-Shaw cells.

ACKNOWLEDGMENTS

We acknowledge the useful discussions with Nicolas Périnet. This work is partly supported by the National Natural Science Foundation of China (Approval Nos. 11272209, 11432009, and 11702099) and the China Postdoctoral Science Foundation (Approval No. 2017M612670).

APPENDIX: EXPERIMENTAL DATA

TABLE II. Wave lengths and wave heights measured in laboratory experiments. Each variable is measured five times.

$d(\text{mm})$	$F(\text{m/s}^2)$	$f(\text{Hz})$	Wave length $\lambda(\text{mm})$						Wave height $H(\text{mm})$			
10	14	18	24.90	24.63	24.20	24.66	24.35	8.92	9.15	9.22	9.02	8.73
		19	22.54	22.76	22.47	22.71	22.69	8.88	8.07	8.17	8.07	9.02
		20	20.41	20.63	20.65	20.47	20.67	7.51	7.43	7.46	7.43	7.34
		21	18.25	18.16	18.33	18.42	18.30	7.18	7.07	7.08	7.13	7.13
		22	16.56	16.70	16.11	16.55	16.48	6.20	6.53	6.81	6.48	6.60
		23	16.19	16.24	16.34	16.28	16.19	5.24	5.50	5.63	5.71	5.12
		24	16.07	15.83	15.93	16.11	15.98	4.88	5.00	4.96	5.43	5.34
20	14	18	25.33	24.49	24.12	24.66	24.97	8.98	9.37	9.55	9.32	9.41
		19	22.20	22.19	22.47	22.34	22.37	8.42	8.48	8.33	8.37	8.44
		20	20.67	20.59	20.64	20.74	20.81	7.59	7.64	7.56	7.66	7.69
		21	19.31	19.22	19.41	19.52	19.33	6.74	7.10	6.78	6.82	6.87
		22	17.17	17.96	17.45	17.65	17.74	6.47	6.03	6.36	6.27	6.22
		23	17.14	16.54	17.06	17.09	17.21	5.42	5.71	5.47	5.56	5.57
		24	15.73	16.04	15.48	15.92	15.97	5.10	4.94	5.30	5.18	5.06
30	12	18	23.04	23.62	23.66	23.63	23.94	8.61	8.24	8.14	8.32	8.29
		19	21.85	21.94	21.87	21.91	22.04	7.21	7.24	7.23	7.32	7.16
		20	20.32	20.39	20.41	20.29	20.31	6.42	6.38	6.30	6.33	6.39
		21	18.45	19.10	18.49	19.07	18.93	5.94	5.63	6.02	5.99	5.91
		22	17.94	17.97	17.98	17.95	17.78	4.93	5.51	4.98	5.11	5.14
		23	16.51	16.96	16.90	16.67	16.81	4.69	4.43	4.48	4.54	4.49
		24	15.66	15.94	16.02	15.87	15.92	4.19	3.87	3.98	4.05	4.03

TABLE III. Wave lengths and wave heights measured in laboratory experiments. Each variable is measured five times.

d (mm)	F (m/s ²)	f (Hz)	Wave length λ (mm)					Wave height H (mm)				
10	20	10	19.66	19.70	19.71	19.77	19.59	4.84	5.50	5.39	5.38	5.34
		11	20.34	20.27	19.73	19.73	20.34	5.67	5.52	5.99	6.02	5.81
		12	20.37	20.39	19.73	20.48	20.46	6.27	6.38	6.74	6.36	6.37
		13	19.31	19.27	20.65	20.49	19.37	7.42	7.47	6.80	6.89	7.46
		14	19.39	19.68	19.35	19.47	20.80	7.95	7.88	8.02	7.97	7.33
		15	21.07	21.16	19.56	19.54	20.83	7.75	7.75	8.37	8.47	7.84
		16	20.75	21.62	21.53	19.95	21.40	8.32	7.95	8.11	8.70	8.12
		17	22.93	21.92	22.72	22.55	22.93	7.84	8.40	7.91	7.91	7.79
		18	23.15	21.89	23.16	23.66	23.33	8.22	8.65	8.30	7.93	8.15
20	20	9	20.29	20.29	20.25	20.22	20.31	4.32	4.27	4.21	4.19	4.26
		10	20.28	20.32	20.23	20.33	20.31	5.31	5.23	5.18	5.16	5.29
		11	20.34	20.39	20.45	20.33	20.49	5.91	5.85	5.86	5.82	5.88
		12	19.36	20.39	20.52	20.11	20.08	7.18	6.57	6.43	6.72	6.68
		13	19.79	20.35	20.57	20.14	20.31	7.47	7.13	6.97	7.11	7.09
		14	19.39	20.50	20.63	19.67	19.97	8.08	7.59	7.52	7.69	7.62
		15	21.12	20.76	20.65	20.55	20.94	7.82	8.05	8.04	7.91	7.89
		16	21.79	20.69	21.07	21.03	21.14	8.03	8.55	8.42	8.33	8.41
		17	22.39	22.15	22.58	22.23	22.19	8.31	8.35	8.29	8.34	8.39
30	20	10	19.66	19.57	19.59	19.69	19.62	5.52	5.46	5.79	5.71	5.44
		11	19.47	19.55	19.54	19.58	19.38	6.12	6.45	6.19	5.94	5.86
		12	19.55	19.58	19.46	19.62	19.71	6.63	6.51	6.39	6.56	6.41
		13	19.96	20.11	19.65	20.34	19.98	6.99	7.11	7.07	6.87	6.93
		14	20.62	20.69	20.24	20.43	20.55	7.98	7.71	7.84	8.13	8.09
		15	20.77	20.71	20.61	20.57	20.77	7.88	7.95	8.02	7.94	8.07
16	21.13	20.77	20.95	21.19	21.06	7.85	7.74	7.61	8.04	7.91		

- ¹M. Faraday, "On a peculiar class of acoustical figures; and on certain forms assumed by groups of particles upon vibrating elastic surfaces," *Philos. Trans. R. Soc. London* **121**, 299–340 (1831).
- ²L. Matthiessen, "Akustische versuche, die kleinsten transversalwellen der flüssigkeiten betreffend," *Ann. Phys. Chem.* **210**, 107–117 (1868).
- ³Lord Rayleigh, "VII. On the crispations of fluid resting upon a vibrating support," *London, Edinburgh, Dublin, Philos. Mag. J. Sci.* **16**, 50–58 (1883).
- ⁴T. B. Benjamin and F. Ursell, "The stability of the plane free surface of a liquid in vertical periodic motion," *Proc. R. Soc. A* **225**, 505–515 (1954).
- ⁵J. Miles and D. Henderson, "Parametrically forced surface waves," *Annu. Rev. Fluid Mech.* **22**, 143–165 (1990).
- ⁶A. V. Kityk, J. Embs, V. V. Mekhonoshin, and C. Wagner, "Spatiotemporal characterization of interfacial Faraday waves by means of a light absorption technique," *Phys. Rev. E* **72**, 036209 (2005).
- ⁷M. C. Cross and P. C. Hohenberg, "Pattern formation outside of equilibrium," *Rev. Mod. Phys.* **65**, 851 (1993).
- ⁸E. Bosch, H. Lambermont, and W. van de Water, "Average patterns in Faraday waves," *Phys. Rev. E* **49**, R3580 (1994).
- ⁹J. Rajchenbach, A. Leroux, and D. Clamond, "New standing solitary waves in water," *Phys. Rev. Lett.* **107**, 024502 (2011).
- ¹⁰X. Li, D. Xu, and S. Liao, "Observations of highly localized oscillons with multiple crests and troughs," *Phys. Rev. E* **90**, 031001 (2014).
- ¹¹X. Li, Z. Yu, and S. Liao, "Observation of two-dimensional Faraday waves in extremely shallow depth," *Phys. Rev. E* **92**, 033014 (2015).
- ¹²N. Perinet, C. Falcon, J. Chergui, and D. Juric, "Hysteretic Faraday waves," *Phys. Rev. E* **93**, 063114 (2016).
- ¹³S. Ubal, M. D. Giavedoni, and F. A. Saita, "A numerical analysis of the influence of the liquid depth on two-dimensional Faraday waves," *Phys. Fluids* **15**, 3099 (2003).
- ¹⁴K. Kumar and L. S. Tuckerman, "Parametric instability of the interface between two fluids," *J. Fluid Mech.* **279**, 49 (1994).
- ¹⁵S. Afkhami and Y. Renardy, "A volume-of-fluid formulation for the study of co-flowing fluids governed by the Hele-Shaw equations," *Phys. Fluids* **25**, 082001 (2013).
- ¹⁶P. Gondret and M. Rabaud, "Shear instability of two-fluid parallel flow in a Hele-Shaw cell," *Phys. Fluids* **9**, 3267 (1997).
- ¹⁷P. Gondret, P. Ern, L. Meignin, and M. Rabaud, "Experimental evidence of a nonlinear transition from convective to absolute instability," *Phys. Rev. Lett.* **82**, 1442–1445 (1999).
- ¹⁸E. Talib, S. V. Jalikop, and A. Juel, "The influence of viscosity on the frozen wave instability: Theory and experiment," *J. Fluid Mech.* **584**, 45–68 (2007).
- ¹⁹J. Rajchenbach and D. Clamond, "Faraday waves: Their dispersion relation, nature of bifurcation and wave number selection revisited," *J. Fluid Mech.* **777**, R2 (2015).
- ²⁰C. Ruyer-Quil, "Inertial corrections to the Darcy law in a Hele-Shaw cell," *C. R. Acad. Sci., Ser. IIb: Mech.* **329**, 337–342 (2001).
- ²¹J. U. Brackbill, D. B. Kothe, and C. Zemach, "A continuum method for modeling surface tension," *J. Comput. Phys.* **100**, 335–354 (1992).
- ²²S. Popinet, "Gerris: A tree-based adaptive solver for the incompressible Euler equations in complex geometries," *J. Comput. Phys.* **190**(2), 572–600 (2003).
- ²³S. Popinet, "An accurate adaptive solver for surface-tension-driven interfacial flows," *J. Comput. Phys.* **228**(16), 5838–5866 (2009).
- ²⁴P.-Y. Lagrée, L. Staron, and S. Popinet, "The granular column collapse as a continuum: Validity of a two-dimensional Navier-Stokes model with a $\mu(I)$ -rheology," *J. Fluid Mech.* **686**, 378–408 (2011).
- ²⁵J. Hoepffner, R. Blumenthal, and S. Zaleski, "Self-similar wave produced by local perturbation of the Kelvin-Helmholtz shear-layer instability," *Phys. Rev. Lett.* **106**, 104502 (2011).
- ²⁶D. Fuster, J.-P. Matas, S. Marty, S. Popinet, J. Hoepffner, A. Cartellier, and S. Zaleski, "Instability regimes in the primary breakup region of planar coflowing sheets," *J. Fluid Mech.* **736**, 150–176 (2013).
- ²⁷L. Deike, D. Fuster, M. Berhanu, and E. Falcon, "Direct numerical simulations of capillary wave turbulence," *Phys. Rev. Lett.* **112**, 234501 (2014).

- ²⁸J. Bouchgl, S. Aniss, and M. Souhar, “Interfacial instability of two superimposed immiscible viscous fluids in a vertical Hele-Shaw cell under horizontal periodic oscillations,” *Phys. Rev. E* **88**, 023027 (2013).
- ²⁹D. M. Henderson and J. W. Miles, “Surface-wave damping in a circular cylinder with a fixed contact line,” *J. Fluid Mech.* **275**, 285–299 (1994).
- ³⁰B. Christiansen, P. Alstrom, and M. T. Levinsen, “Dissipation and ordering in capillary waves at high aspect ratios,” *J. Fluid Mech.* **291**, 323–341 (1995).
- ³¹P. Chen and J. Vinals, “Amplitude equation and pattern selection in Faraday waves,” *Phys. Rev. E* **60**, 559–570 (1999).
- ³²G. Acar and B. F. Feeny, “Floquet-based analysis of general responses of the Mathieu equation,” *J. Vib. Acoust.* **138**, 041017 (2016).
- ³³X. Li, X. Li, and S. Liao, “Pattern transition of two-dimensional Faraday waves at an extremely shallow depth,” *Sci. China: Phys., Mech. Astron.* **59**, 114712 (2016).